Applied Catalysis B: Environmental 343 (2024) 123540

Contents lists available at ScienceDirect

Applied Catalysis B: Environmental

journal homepage: www.elsevier.com/locate/apcatb

Vanadium in strongly correlated electron system $Ni_{1-x}V_xWO_4$: Paradoxically boosted $deNO_x$ reaction under SO_x environment via modulating electron correlation

June Won Suh [a,1], Jihye Park [b,1], Si Hoon Jeong [a], Gi Hyun Park [a], Myung Sik Choi [c], Changhyun Jin [a], Jung-Woo Lee [d], Kimoon Lee [e], Bo Ra Jeong [f], Hong-Dae Kim [f], Sun-Dong Kim [g], Hak Joo Kim [g], Sung Eun Kim [g], Yunseong Ji [h,i], Hyesung Lee [h], Joonho Bang [b,j,*], Kyu Hyoung Lee [a,**], Seung Yong Lee [a,i,***]

[a] Department of Materials Science and Engineering, Yonsei University, Seoul 03722, Republic of Korea
[b] Department of Materials Engineering and Convergence Technology, Gyeongsang National University, Jinju 52828, Republic of Korea
[c] School of Nano & Materials Science and Engineering, Kyungpook National University, Sangju 37224, Republic of Korea
[d] Department of Materials Science and Engineering, Hongik University, Sejong 30016, Republic of Korea
[e] Department of Physics, Kunsan National University, Gunsan 54150, Republic of Korea
[f] Green Materials and Processes R&D Group, Korea Institute of Industrial Technology, Ulsan 44413, Republic of Korea
[g] Korea Institute of Energy Research, 152 Gajeong-ro, Yuseong-gu, Daejeon 34129, Republic of Korea
[h] Department of Chemical and Biomolecular Engineering, Yonsei University, 50 Yonsei-ro, Seodaemun-gu, Seoul 03722, Republic of Korea
[i] KIURI Institute, Yonsei University, Seoul 03722, Republic of Korea
[j] School of Materials Science and Engineering, Gyeongsang National University, Jinju 52828, Republic of Korea

ARTICLE INFO

Keywords:
Denitration
SO_x tolerance
Selective catalytic reduction
$Ni_{1-x}V_xWO_4$
Strongly correlated electron system

ABSTRACT

The persistent challenge of NO_x selective catalytic reduction degradation in the presence of SO_x has remained unresolved for decades. In this study, we report a paradoxical boosted denitration performance more than 20% under the SO_x environment through controlling the charge state of V utilizing strongly correlated electron systems (SCES) in $Ni_{1-x}V_xWO_4$. Substitutional doped V at the Ni site, and the computed charge gap from DFT confirms the SCES. Through the manipulation of the strong correlation between V and Ni, V preserves the between + 2–3 charge state in the presence of SO_x. Furthermore, we achieved a stable oxidation/reduction cycle and higher denitration efficiency by altering the oxidation point of $(NH_4)HSO_4$-contaminated $Ni_{1-x}V_xWO_4$. This results from deliberate decrease in Coulombic repulsion between Ni and V, improving electron transfer for catalytic performance. This revelation offers a resolution of exceptional denitration performance within SO_x in industrial exhaust systems, exploiting the foundational principles of SCES.

1. Introduction

The utilization of selective catalytic reduction (SCR) has become prevalent in the mitigation of nitrogen oxide (NO_x) emissions from exhaust systems in thermal power plants and internal combustion engines. By employing urea ($CO(NH_2)_2$) or ammonia (NH_3), NOx is converted to nitrogen (N_2) and water (H_2O) on metal oxide (MO) catalysts like V_2O_5, achieved through modulation of valence states between V^{+2} and V^{+5}. Therefore, numerous studies have delved into strategies to enhance SCR efficiency, encompassing catalyst doping, pore size modulation, and surface modifications to maximize NH_3 and NO_x adsorption on MO catalysts [1–7]. However, the enduring challenge of NO_x selective catalytic reduction degradation in the presence of sulfur oxides (SO_x), inevitably stemming from fossil fuel combustion, has remained unsolved [2]. The deposition of ammonium bisulfates salt (ABS, $(NH_4)HSO_4$) due to NH_3-SO_x interactions on the catalyst obstructs acid sites,

* Corresponding author at: Department of Materials Engineering and Convergence Technology, Gyeongsang National University, Jinju 52828, Republic of Korea.
** Corresponding author.
*** Corresponding author at: Department of Materials Science and Engineering, Yonsei University, Seoul 03722, Republic of Korea.
E-mail addresses: bang@gnu.ac.kr (J. Bang), khlee2018@yonsei.ac.kr (K.H. Lee), lsy549@yonsei.ac.kr (S.Y. Lee).
[1] These authors contributed equally.

https://doi.org/10.1016/j.apcatb.2023.123540
Received 19 September 2023; Received in revised form 17 November 2023; Accepted 19 November 2023
Available online 21 November 2023
0926-3373/© 2023 Elsevier B.V. All rights reserved.

leading to disruption of the reduction/oxidation cycle and a significant reduction in $deNO_x$ efficiency. In addition, synthesized ABS physically obstructs the catalyst surface [1,8]. Despite decades of extensive efforts to enhance SO_x tolerance, the degradation of $deNO_x$ performance continues to persist. Hence, alternative perspectives are imperative. Several proposed solutions have suggested mitigating the impact of SO_x on SCR catalysts through diverse approaches, including enhancing catalyst stability via optimized supports, combining various catalytic materials, exploring alternative catalytic substances, customizing exhaust gas decreasing systems, acid site control, sulfation, and adding purifying process under higher temperatures [8–18]. Given these extensive efforts, overcoming these limitations requires a different vantage point. From the research findings, we have gleaned insights into the potential of non-overlapping cation oxidation states or the inhibition of metal sulfates, even when they are enveloped by ABS, suggesting the achievement of a stable catalytic cycle beyond the conventional MO behavior. As a result, our focus lies on intriguing materials with high barriers to carrier transfer and the exposure of *d*-electron cation catalyst sites differing from the activated catalytic site of weaker oxygen bonding in V_2O_5.

In this context, we embrace the concept of strongly correlated electron systems (SCES) insulators, characterized by strong Coulombic repulsion between electrons in cations, resulting in manifold degrees of freedom arising from electron correlations and yielding tailorable electronic, magnetic, and optical properties [19,20]. These interactions, which amalgamate electron-electron repulsion and principles of quantum mechanics, serve as the foundation for magnetic order an aspect of significant technological and physical relevance. The pronounced strong Coulombic repulsion facilitates carrier transfer via hopping of localized (*d* or *f*-orbital) electrons between nearest cations described as $i^n j^n \rightarrow i^{n-1} j^{n+1}$ (i and j are different cations). Consequently, the diverse mechanisms of carrier transfer in SCES insulators, as opposed to conventional transition metal oxide ($i^n O^n \rightarrow i^{n+1} O^{n-1}$, where i and O are the cation and oxygen), demonstrate the prospective application of various fields by modifying crystal structure and composition via the tuning of Coulomb repulsion between *d* electron cations [21–24]. In SCES catalysts, the weakening of the electron correlations induced enhancements in conductivity, thereby improving charge transfer at catalyst–product interfaces to elevate the performance of catalysts [19,25–28]. This motivates the modulation of SCES correlation control through strategies such as applying strain to the matrix or distorting the crystal structure via compositional doping, all in the pursuit of catalytic site activation.

In this study, we aim to enhance electron transfer between nearest cations to activate catalytic sites, particularly when lower correlations between cations are obstructed by ABS on V-doped $NiWO_4$ SCES insulators. The $NiWO_4$ SCES insulator features a monoclinic structure with lower symmetry than cubic NiO, offering an additional degree of freedom compared to binary SCES insulators. It features approximately 4 Å of vacant space within its crystal lattice. The substitutionally doped V is located at the $[NiO_6]$ octahedral site, mirroring the + 2.x persistent valence state of V and associated with the Coulombic repulsion of Ni. The V atoms within the $NiWO_4$ SCES matrix emerge SCR activity due to the diluted electron correlation of each magnetic cation within uncontaminated environments. Simultaneously, elevated SCR performance is observed when the surface of $Ni_{1-x}V_xWO_4$ (x = 0.05, 0.1) is tainted by ABS. The V dopant maintains its + 2.α valence state due to sustained electron correlation with Ni. However, heightened carrier transfer transpires under ABS-induced strong acidification, driven by higher electron/hole pair as $Ni^{+2.\alpha}V^{+2.\alpha} \rightarrow Ni^{+2.\alpha-\gamma}V^{+2.\alpha+\delta}$, promoting an enhanced exchange of carriers between NH_3 gas and higher adsorption on $Ni_{1-x}V_xWO_4$ surfaces. Furthermore, the creation of oxidation sites generates a sustainable reduction/oxidation cycle, contributing to stable catalytic activity. This process, in turn, leads to boosted $deNO_x$ performance in the presence of SO_x on SCES oxide of $Ni_{1-x}V_xWO_4$. The paradoxically elevated catalytic efficiency observed on ABS-contaminated surfaces, achieved through tuning electron correlation, introduces an unprecedented solution for advanced SCR catalysts – a field that has hitherto been hindered by inescapable atmospheric conditions.

2. Experiment section

2.1. Synthesize the sample and structure analysis

The $NiWO_4$, $V_{0.05}Ni_{0.95}WO_4$, and $V_{0.1}Ni_{0.9}WO_4$ powders were synthesized by solid-state reactions. The metal oxide powders, NiO, WO_3, and V_2O_5, were mixed following the stoichiometric ratios of each composition. Subsequently, a calcination process was carried out in an electric furnace at 700 °C for 12 h. Additionally, the fabrication of ABS-contaminated samples involved combining 10 wt% of ABS with DI water. After drying the mixture was overnight in an oven, heat treatment at 100 °C for 3 h was administered. Crystal structure analysis of synthesized powder was conducted using X-ray diffractometer (XRD) and Fourier transform infrared (FT-IR) spectroscopy. The XRD results were obtained using the Rigaku Smartlab system, recording spectra with the angular (2θ) range of 20 – 80 degrees by via Kα1 radiation of copper (λ = 1.54059 Å). The detailed structures were refined using GSAS-2, and the resulting crystal structures were visualized using VESTA. [29,30] Polarity and dipole vibration mode measurements were acquired via FT-IR spectroscopy (Vertex 70, Bruker, United States). Subsequently, a comprehensive analysis of the microstructure and morphology was performed using scanning electron microscopy (SEM, JEOL JSM-7001 F, Japan) operating at an acceleration potential of 17 kV. Elemental mapping was accomplished through the utilization of energy-dispersive X-ray spectroscopy (EDS).

2.2. Measurement of physical and chemical characteristics

The optical band gap was determined using ultraviolet-visible and near-infrared diffuse reflectance spectroscopy (UV–VIS–NIR DRS, Cary5000, Agilent Technologies, United States). Magnetic properties were characterized using superconducting quantum interference device vibrating sample magnetometer (Squid-VSM, Quantum Design). Elemental oxidation states were elucidated through X-ray photoelectron spectroscopy (XPS, K-alpha, Thermo Fisher Scientific, United States). Impedance measurements were conducted using potentiostat (VSP potentiostat, Bio-logic). For temperature-programmed experiments, including reduction (TPR), desorption (TPD), and oxidation (TPO), were conducted using an AutoChem II 2920 (Micromeritics Instrument Corp., USA). Prior to TPR/ TPO measurements, a heat treatment step at 200 °C for 30 min was employed to eliminate H_2O and NH_3 absorption. TPD measurements were conducted at 50 °C for 60 min. The purging process was carried out at 50 °C for 1 h, followed by Ar purging for another 1 h.

2.3. Calculation of electronic structure

First-principles density functional theory (DFT) calculations were conducted utilizing the projector-augmented-wave method, employing the Perdew–Burke–Ernzerhof functional as implemented in the Vienna Ab initio simulation program (VASP) code [31–33]. The valence electrons employed in the calculations encompassed the 3*d* and 4 *s* electrons of Ni, 5*d* and 6 *s* electrons of W, 2 *s* and 2*p* electrons of O, and 3*d* and 4 *s* electrons of V. To capture the effects of localized electrons, an on-site Coulomb interaction was incorporated, utilizing a simplified rotationally invariant approach [34]. The Coulomb *U* and exchange *J* parameters, $U_{eff} = U - J$, and a value of 5.3 eV were chosen for the Ni 3*d* and V 3*d* orbitals [35,36]. A plane-wave basis cut-off energy of 800 eV was employed. For the partial substitution of V on the Ni site, a supercell with dimensions of $a \times b \times 2c$ was employed. The k-point meshes adopted were 2 × 4 × 4 and 2 × 4 × 2 for the unit cell and supercell, respectively. Structural relaxation was conducted iteratively until the Hellmann–Feynman forces reached a convergence threshold of less than 1×10^{-3} eV $Å^{-1}$.

2.4. Catalytic activity evaluation

The fixed bed deNOx performance assessment was executed by KITECH. The catalytic performance was evaluated in a fixed-bed reactor under atmospheric pressure. The operating temperature varied from 100 °C to 300 °C, and measurements were conducted for 40 min per data point. The reactive gas consisted 500 ppm of NO_x, NH_3, 100 ppm of SO_x, and 10 vol% of O_2, with the remaining balance being N_2, at a total flow rate of 500 sccm. For the evaluation, 0.35 mg of powdered catalyst was prepared, resulting in a gas hourly space velocity (GHSV) of 60,000 h^{-1}. Reactive gas concentrations were continuously monitored using FTIR spectroscopy (CX–4000; Gasmet Technologies, Vantaa, Finland) and an O_2 analyzer (Oxitec 5000; ENOTEC, Marienheide, Germany).

The NO_x conversion and N_2 selectivity were calculated in terms of the following formulas

$$NO_x \quad conversion(\%) = \frac{[NO]_{in} - [NO]_{out}}{[NO]_{in}} \times 100$$

$$N_2 \ selectivity(\%) = \frac{[NO]_{in} - [NO]_{out} + [NH_3]_{in} - [NH_3]_{out} - [NO_2]_{out} - [N_2O]_{out}}{[NO]_{in} - [NO]_{out} + [NH_3]_{in} - [NH_3]_{out}} \times 100$$

3. Results and discussion

3.1. Boosted deNO$_x$ reaction under SO$_x$ environment absorption

XRD results of $Ni_{1-x}V_xWO_4$ samples in Fig. S1 synthesized by using solid-state reactions demonstrate the single phase of $Ni_{0.95}V_{0.05}WO_4$, $Ni_{0.9}V_{0.1}WO_4$, but the impurities phase of peaks exhibit in $Ni_{0.85}V_{0.15}WO_4$ composition due to the limitation of V solubility in $NiWO_4$ matrix. We measured deNO$_x$ performance under SO$_x$ using a single phase of $Ni_{0.95}V_{0.05}WO_4$, $Ni_{0.9}V_{0.1}WO_4$, and mixed V_2O_5-WO_3 compounds from 100 °C to 300 °C of temperature range for all samples, as shown in Fig. 1a and Fig. S2. The V_2O_5-WO_3 compound exhibited a deteriorated deNO$_x$ performance in the presence of SO$_x$ (see Fig S2). In contrast, $Ni_{1-x}V_xWO_4$ represented an unusual deNO$_x$ catalytic reaction, as displayed in Fig. 1a. In the absence of SO$_x$ (depicted by open circles),

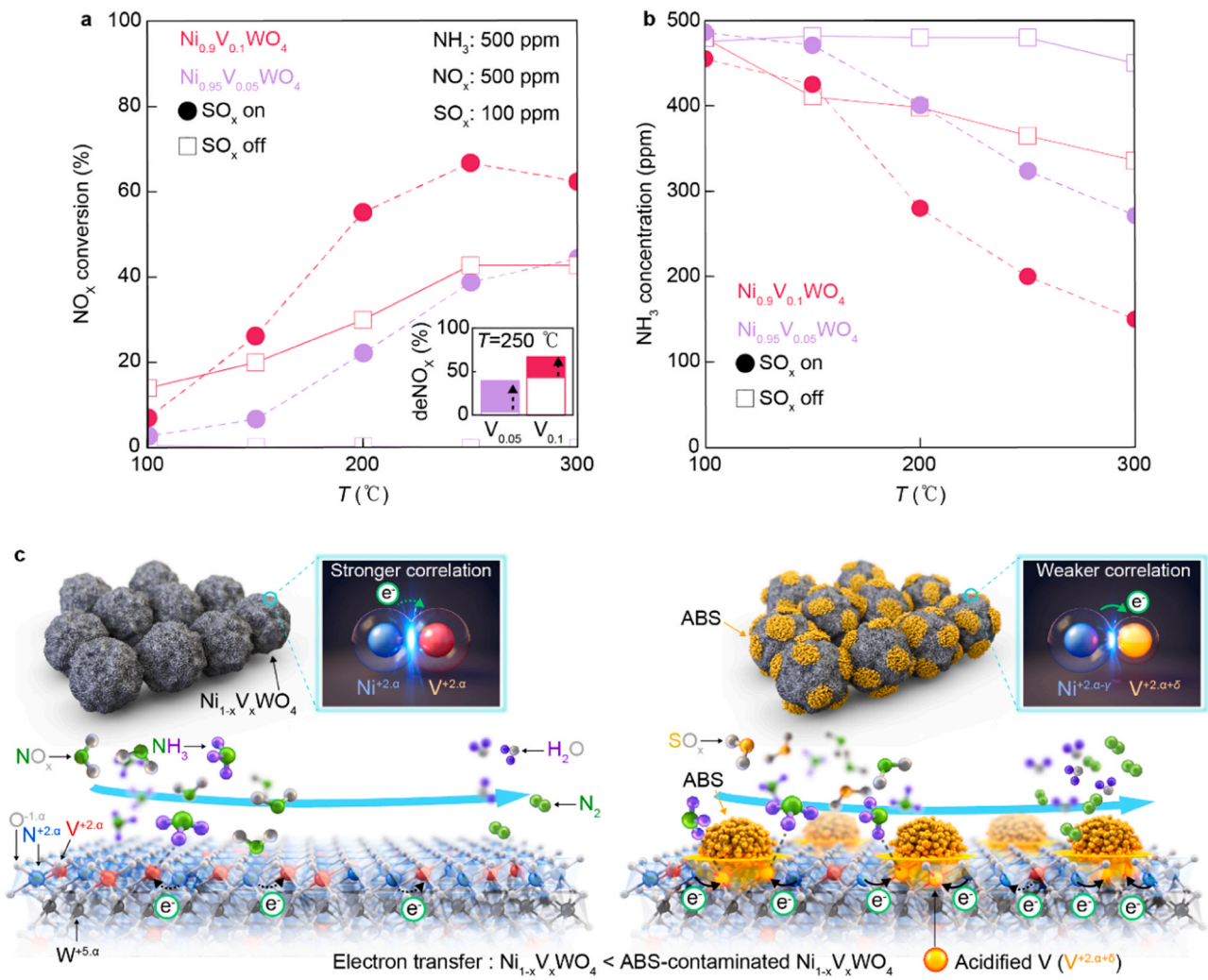

Fig. 1. Boosted deNO$_x$ performance under SO$_x$ environment on $Ni_{1-x}V_xWO_4$. (a) NO$_x$ conversion performance with SO$_x$ on (closed circle) and SO$_x$ off (open square) environment. The enhanced deNO$_x$ performance at 250 °C is shown in the inset plot. Detailed results on time-dependent deNO$_x$ performance under SO$_x$ can be found in Fig. S3. (b) Plot showing NH_3 concentration changes at different temperatures. Solid squares represent conditions under SO$_x$, while open squares represent conditions without SO$_x$. (c) The schematic illustrates the mechanism of boosted deNO$_x$ reaction in the presence of SO$_x$ on ABS-contaminated $Ni_{1-x}V_xWO_4$ particles. The lower electron transfer on the clean surface (left) and the higher activated electron transfer on the ABS-contaminated $Ni_{1-x}V_xWO_4$ (right) depend on the correlation strength between Ni (blue atoms) and V (red atoms). The weaker correlation between $Ni^{+2.\alpha-\gamma}$ acidified V (orange atoms, $V^{+2.\alpha+\delta}$) in ABS-contaminated particles exhibits higher NH_3 adsorption than $V^{+2.x}$ due to higher activated carrier transfer to $V^{+2.\alpha+\delta}$.

$Ni_{0.9}V_{0.1}WO_4$ demonstrated more than a 20% conversion of NO_x around 250 °C, which then increased to approximately 40% conversion up to 300 °C. However, the inactive catalytic response in $Ni_{0.95}V_{0.05}WO_4$ can be attributed to its higher band-gap compared to $Ni_{0.9}V_{0.1}WO_4$. It is noted that the $deNO_x$ performance was significantly enhanced in the presence of SO_x at 200 – 300 °C (indicated by closed circles). The inset of Fig. 1a shows a more than 20% improvement in the catalytic reaction when $Ni_{0.9}V_{0.1}WO_4$ is exposed to SO_x poisoning. The NH_3 adsorption on the catalyst surface (Fig. 1b) revealed accordance with the NO_x conversion behavior of $Ni_{1-x}V_xWO_4$. The substantial reduction in NH_3 concentration under both SO_x and constant SO_x concentration (Fig. S4a) suggests a contradictory higher adsorption of NH_3 without concurrent SO_x adsorption on the $Ni_{1-x}V_xWO_4$ surface. The N_2 selectivity (Fig. S4b) exhibited over 95% on both clean and poisoned $Ni_{0.9}V_{0.1}WO_4$ surfaces. Particularly noteworthy is the low N_2 selectivity and NO_x conversion on the clean $Ni_{0.95}V_{0.05}WO_4$, which experienced enhancement under SO_x conditions, suggesting distinct catalytic mechanisms between clean and ABS-contaminated surfaces. This abnormal $deNO_x$ performance observed in this study signifies a distinct catalytic reaction in SCES materials, setting them apart from conventional MOs such as V_2O_5, MnO, and Cu-zeolites, which typically exhibit degraded NO_x conversion in the presence of SO_x, as demonstrated in numerous reports [8–16]. In conventional SCR catalysts, the catalytic sites are physically obstructed by ABS, and the higher acidified V leads to reduced NO_x conversion due to lower NH_3 absorption, resulting in an unstable reduction/oxidation cycle. However, our report showcases boosted $deNO_x$ performance in ABS-contaminated $Ni_{1-x}V_xWO_4$ SCES materials, achieved by manipulating the V valence state between + 2 – + 3 through $Ni^{+2.\alpha}$ in the SCES $NiWO_4$ matrix (Fig. 1c). In this system, V predominantly serves as the catalytic site in $NiWO_4$ for NH_3 adsorption and forms a strong correlation with $Ni^{+2.\alpha}$, inducing a valence state of $V^{+2.\alpha}$. In SCES materials with electron hopping paths between cations, the symmetric electron/hole pair of $Ni^{+2.\alpha}$ and $V^{+2.\alpha}$ leads to lower carrier transfer in pristine $Ni_{1-x}V_xWO_4$, resulting in poor $deNO_x$ performance in terms of NH_3 absorption. Paradoxically, the boosted $deNO_x$ performance with higher NH_3 adsorption on ABS-contaminated $Ni_{1-x}V_xWO_4$ SCES materials arises from increased electron transfer by acidified V, described as $V^{+2.\alpha+\delta}$. The manipulated $V^{+2.\alpha+\delta}$ is associated with the preserved crystal structure of ABS-contaminated $Ni_{1-x}V_xWO_4$, which maintains charge neutrality in the presence of ABS. For example, $Ni_{1-x}V_xWO_4$ can be expressed as $1\text{-}xNi^{+2} + xV^{+2} + W^{+6} + 4O^{-2} = 0$ or $1\text{-}xNi^{+3} + xV^{+3} + W^{+5} + 4O^{-2} = 0$. Therefore, ABS-contaminated $Ni_{1-x}V_xWO_4$, with higher acidified form $V^{+2.\alpha+\delta}$, can be described as $1\text{-}xNi^{+2.\alpha\text{-}\gamma} + xV^{+2.\alpha+\delta} + W^{+5.\alpha} + 4O^{-2} = 0$ to maintain charge neutrality. As a result, $Ni^{+2.\alpha\text{-}\gamma}$ and $V^{+2.\alpha+\delta}$ contribute to weaker electron correlation between $Ni^{+2.\alpha\text{-}\gamma}$ and $V^{+2.\alpha+\delta}$, resulting in increased electron transfer through the asymmetric electron/hole pair between $Ni^{+2.\alpha\text{-}\gamma}$ and $V^{+2.\alpha+\delta}$. This improved electron transfer to V in ABS-contaminated $Ni_{1-x}V_xWO_4$ leads to higher NH_3 adsorption for a boosted $deNO_x$ reaction, even in the presence of physically blocked catalytic sites due to ABS. In the subsequent section, we will introduce the role of V in the SCES matrix of $Ni_{1-x}V_xWO_4$, explaining how it maintains a persistent V valence state and enables a stable reduction/oxidation cycle, even in the presence of SO_x.

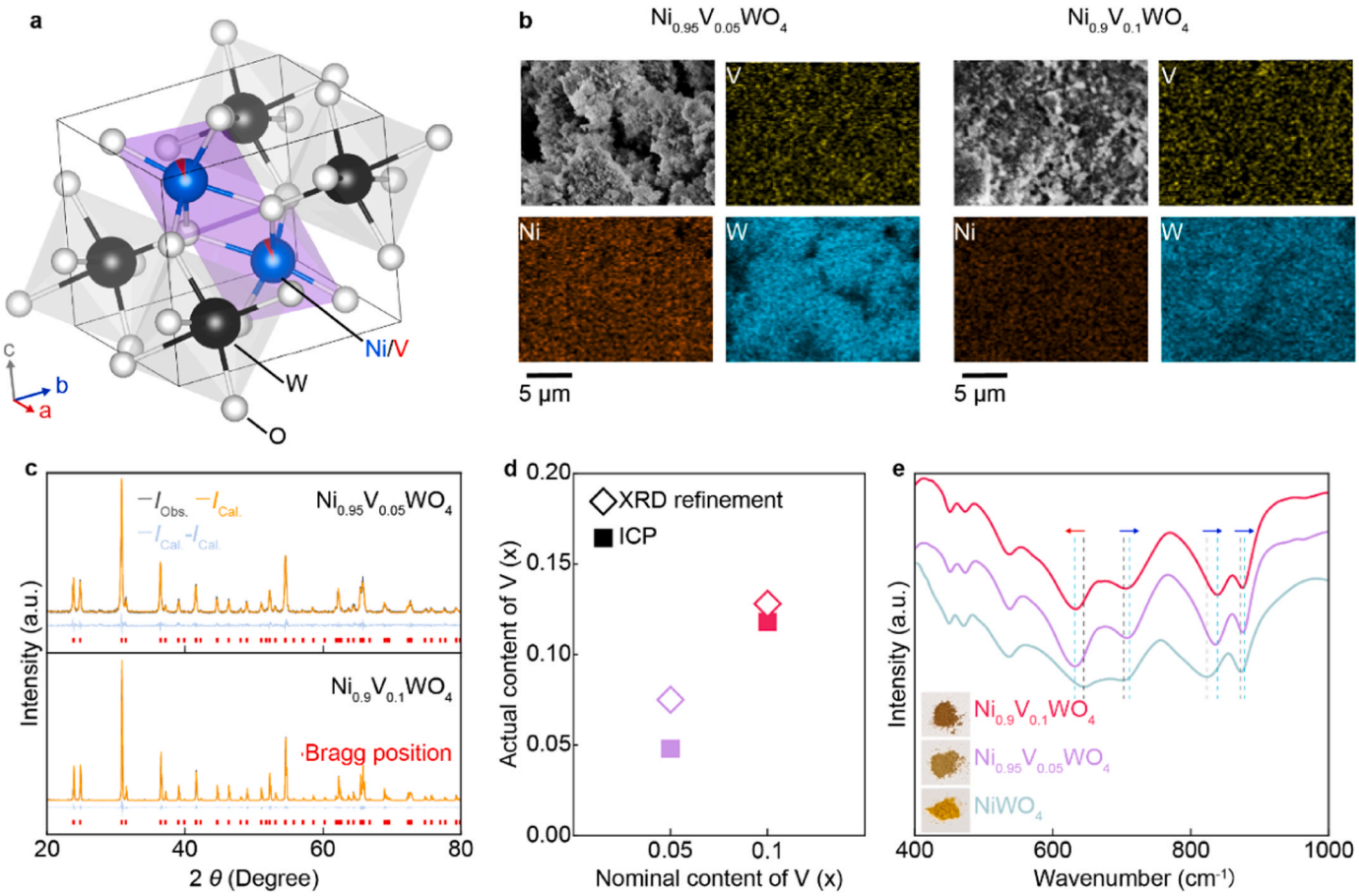

Fig. 2. Structure analysis of $Ni_{1-x}V_xWO_4$. (a) Schematic illustrating the crystal structure of $Ni_{1-x}V_xWO_4$. (b) SEM and EDS mapping results of $Ni_{1-x}V_xWO_4$ powders. (c) XRD Rietveld refinement pattern of powdered $Ni_{1-x}V_xWO_4$. (d) Composition analysis from XRD refinement and ICP. (e) FT-IR results of the $Ni_{1-x}V_xWO_4$ series at the fingerprint region. The peak shift from $NiWO_4$ and $Ni_{1-x}V_xWO_4$ depict as black arrow.

3.2. SCES V-doped $NiWO_4$

The synthesized polycrystalline $Ni_{1-x}V_xWO_4$ powder, prepared through a solid-state reaction, exhibits the P12/c1 space group crystal structure as depicted in Fig. 2a, and was analyzed by XRD Rietveld refinement. The $Ni_{1-x}V_xWO_4$ particles show an even distribution of V within them, as observed in Fig. 2b. The structure of $Ni_{1-x}V_xWO_4$ consists of $[NiO_6]$ and $[WO_6]$ octahedral sublattices, similar to $NiWO_4$, with the substitutionally doped V occupying the Ni site [34–36]. This positioning of V atoms in the $[NiO_6]$ sites is confirmed by both XRD and XPS data. The Rietveld refinement results derived from powder XRD patterns (Fig. 2c) indicate a single phase of V-doped $NiWO_4$ composition, revealing a monotonically increasing a-axis lattice parameter with varying V concentrations (detailed parameter results are shown in Table S1). Additionally, the comparison of XRD pattern intensities in Fig. S5 shows the simulated crystal structures: Model 1 of $Ni_{0.9}V_{0.1}WO_4$ and Model 2 of $NiW_{0.9}V_{0.1}O4$, without any modulation of lattice parameters. Despite sharing the same $NiWO_4$ Bragg positions in all models, different electron densities for each cation (V, Ni, W) result in distinct intensity ratios between the (0 1 1) and (1 1 0) planes. When V is located at the Ni site, the (0 1 1) plane intensity is higher than (1 1 0), whereas it is the opposite when V atoms are located at the W site. Comparing these intensities to the measured XRD pattern of the powder samples, a higher (0 1 1) intensity is observed, aligning with the characteristics of Model 1 of $Ni_{1-x}V_xWO_4$. Furthermore, the XPS data in Fig. S6 represent a binding energy of 512.1 eV, corresponding to the maximum peak position of the V $2p_{3/2}$ for all samples. The deconvolution results indicate a valence state of + 2.α for V. In $NiWO_4$, the valence states of all cations range from + 2 to + 3 for Ni and + 5 to + 6 for W, while O maintains a −2 valence state. Considering the cation valence state derived from the deconvolution results of XPS as $Ni^{+2.\alpha}$ and $V^{+5.\alpha}$, the $V^{+2.\alpha}$ species represent substitutional V atoms in the Ni site within the $Ni_{1-x}V_xWO_4$ structure. The ionic radius of each cation in the 6-coordination of octahedral structure bonding with O is reported as follows:

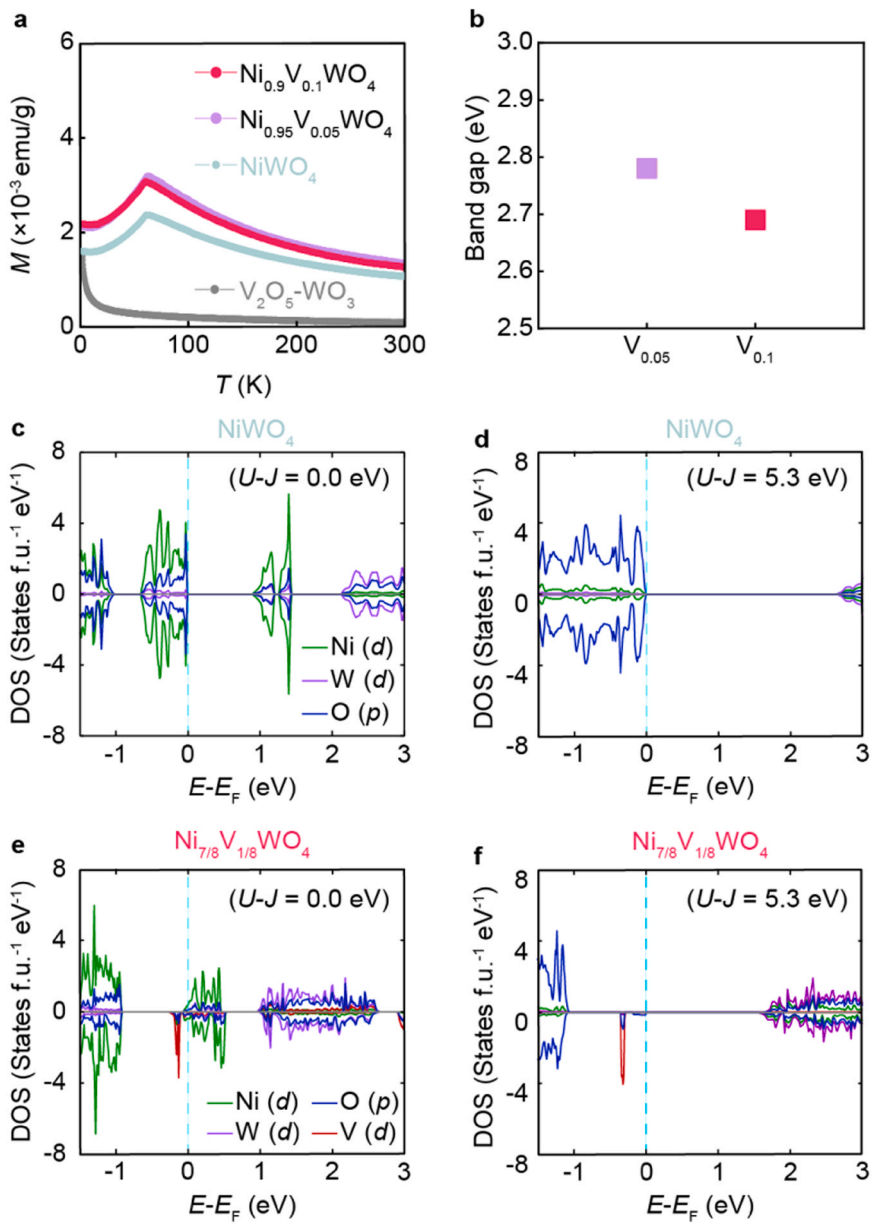

Fig. 3. SCES of $Ni_{1-x}V_xWO_4$ (a) The antiferromagnetic phase of the $Ni_{1-x}V_xWO_4$ series and the paramagnetic phase of the V_2O_5-WO_3 compound. (b) The derived band-gap from UV–vis measurements depends on the amount of V. (c-f) PDOS results of $NiWO_4$ and $Ni_{7/8}V_{1/8}WO_4$ under different *U-J* values(U_{eff}). (c) $NiWO_4$ at U_{eff} = 0 eV. (d) $NiWO_4$ at U_{eff} = 5.3 eV. (e) $Ni_{7/8}V_{1/8}WO_4$ at U_{eff} = 0 eV. (f) $V_{1/8}Ni_{7/8}WO_4$ at U_{eff} = 5.3 eV.

Ni^{+2} 0.69 Å, Ni^{+3} 0.60 – 0.56 Å, W^{+5} 0.62 Å, W^{+6} 0.6 Å, V^{+2} 0.79 Å, and V^{+3} 0.64 Å. These values support the ionic radius of the + 2 to + 3 valence state of V, corresponding to the Ni^{+2-+3} ionic radii when it is substitutionally located in Ni site. The comparison of the V contents derived from XRD refinement and ICP results in Fig. 2d (plotted from Table S2) shows approximately 0.04 and 0.11 V contents from ICP results, and 0.07, 0.13 V contents obtained from XRD refinement. The darker color of $Ni_{1-x}V_xWO_4$ compared to $NiWO_4$ samples in the FT-IR results in Fig. 2e implies the role of V as a carrier dopant in the $NiWO_4$ crystal structure, leading to changes in dipole-dipole interaction, which is reflected in the FT-IR at the fingerprint region [37,38]. The peak shifts (Both of red and blue shift) of FT-IR in Fig. 2e indicate a highly different dipole-dipole interaction between cations when the V atom is doped into $NiWO_4$. Despite altered dipole-dipole interaction due to differing electronegativities between $Ni^{+2.\alpha}$ and $V^{+2.\alpha}$ in $Ni_{1-x}V_xWO_4$, strong repulsion between cations is still evident from magnetic properties measurements.

The temperature-dependence magnetization curve (M-T curve) in Fig. 3a demonstrates the antiferromagnetic phase for all $Ni_{1-x}V_xWO_4$ compositions, similar to SCES $NiWO_4$. The consistent Neel temperature (T_N) across all compositions highlights the strong correlation between cations, such as Ni-Ni and Ni-V. Notably, the magnetic moment of each magnetic cation in $Ni_{1-x}V_xWO_4$ – 3 – 4 μ_B for Ni^{2+}, ~3.0 μ_B for V^{2+}, and ~3.8 μ_B for V^{3+} – results in a net magnetic moment of zero due to antiferromagnetic ordering. This arises from the strong correlation between magnetic cations. The strong Coulombic repulsion between cations leads to substantial charge gap values, which align with theoretical calculations and validate the measured band gaps via UV–vis. The band gap values of $Ni_{1-x}V_xWO_4$ (Fig. 3b) are 2.78 eV for $Ni_{0.95}V_{0.05}WO_4$ and 2.69 eV for $Ni_{0.9}V_{0.1}WO_4$, both of which are lower than the 3.39 eV band gap of the pristine $NiWO_4$ (Fig. S7), that correlated with the change in carrier transfer behavior by V doping. The modulated band structure of $Ni_{1-x}V_xWO_4$ is further substantiated by DFT calculations, as shown in Fig. 3c-f. We performed calculations for intrinsic $NiWO_4$ and $Ni_{7/8}V_{1/8}WO_4$ with effective on-site Coulomb and exchange parameter (U_{eff}) values of 0 and 5.3 eV, signifying the difference between Coulomb parameter (U) and exchange parameter (J). $NiWO_4$ exhibits a ~2.9 eV band gap when the On-site Coulomb interaction is considered, stemming from the strong electron-electron correlation between Ni (d) and aligning with the SCES properties of $NiWO_4$. The ~2.6 eV band gap observed in $Ni_{0.9}V_{0.1}WO_4$ from UV–vis results is in accordance with DFT+U outcomes of $Ni_{7/8}V_{1/8}WO_4$, which displays a band gap of 2.7 eV. With an absence of the band gap from $U_{eff} = 0$ in $Ni_{7/8}V_{1/8}WO_4$, the experimentally synthesized $Ni_{1-x}V_xWO_4$ materials demonstrate a strong electron correlation between cations, leading to the emergence of the band gap in $Ni_{1-x}V_xWO_4$.

3.3. Modulating weaker electron correlation via acidified V

For a comprehensive understanding of the distinctive deNOx results, we conducted reduction-oxidation chemisorption measurements using H_2-TPR, NH_3-TPD, and O_2-TPO in a clean environment of $Ni_{1-x}V_xWO_4$ and V_2O_5-WO_3 compounds (in Fig. 4a-c). The H_2-TPR results in Fig. 4a reveal multiple reduction points in V-doped $NiWO_4$, which is in contrast to the single peak observed in $NiWO_4$ and V_2O_5-WO_3 compounds at around 680 and 700 °C, respectively. These reduction steps signify the transition of ionized cations to a lower valence state, approaching a metallic state through the H_2 reaction. In the case of $Ni_{1-x}V_xWO_4$, an

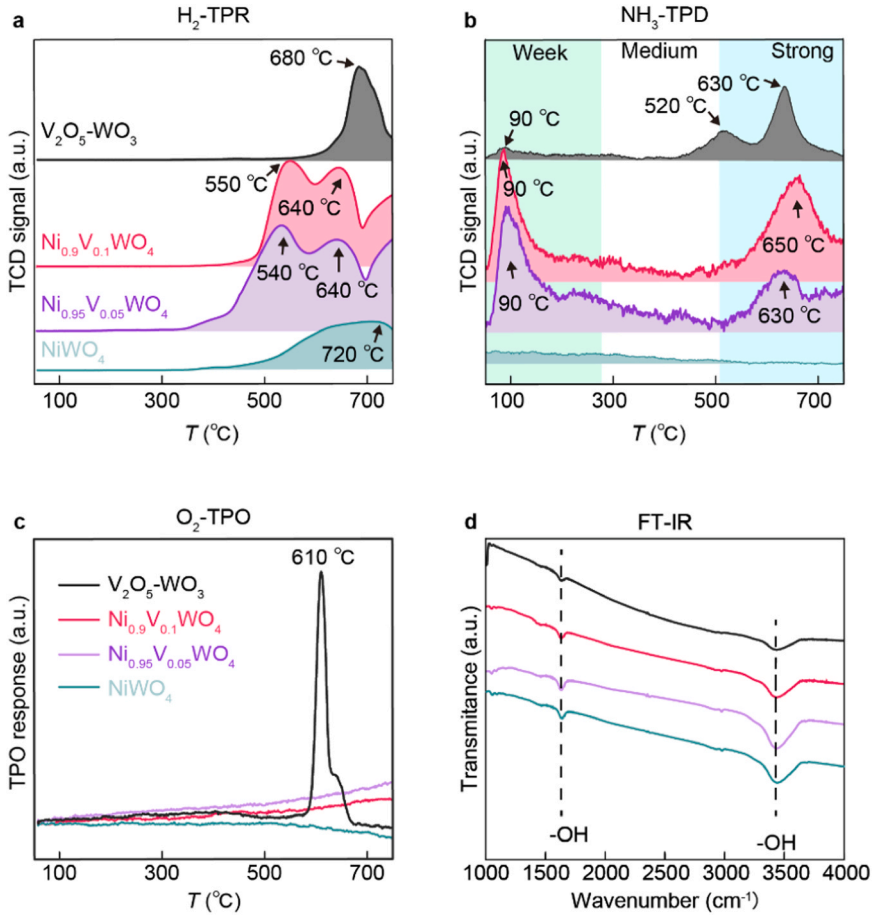

Fig. 4. The chemisorption and FT-IR results of the clean surface of the catalyst sample. (a) H_2-TPR, (b) NH_3-TPD, (c) O_2-TPO results for all samples. (d) FT-IR results of $Ni_{1-x}V_xWO_4$ series and the V_2O_5-WO_3 compound in the 1000 – 40000 cm^{-1} region with indicated -OH group peaks.

additional reduction step is observed due to the presence of substitutional V. The NH_3-TPD measurements depicted in Fig. 4b indicate higher NH_3 desorption around 100 °C for $Ni_{1-x}V_xWO_4$ samples, along with an additional NH_3 adsorption point around 650 °C. The higher $deNO_x$ performance of $Ni_{0.9}V_{0.1}WO_4$ compare to that of $Ni_{0.95}V_{0.05}WO_4$ is considered to be related with lower band gap resulting from weakened Coulombic interaction. The lower NH_3 desorption at the medium acid site corresponds to the relatively weak $deNO_x$ performance around

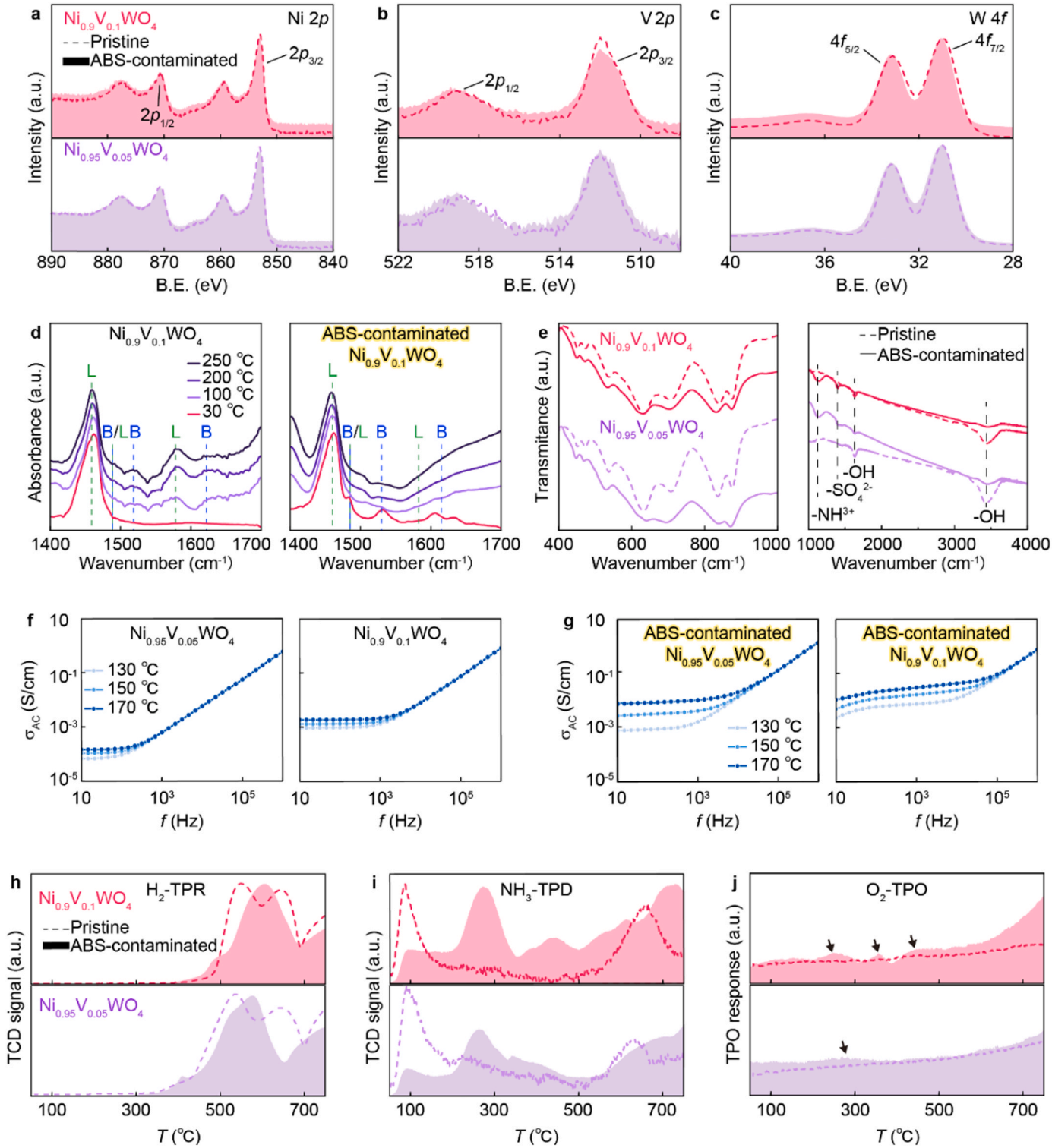

Fig. 5. Weaker electron correlation in ABS-contaminated $Ni_{1-x}V_xWO_4$. (a-c) XPS results with pristine (dotted line) and ABS-contaminated (colored area) for each element such as (a) Ni, (b) V, and (c) W. (Deconvoluted XPS results in noted in Fig. S8.) (d) Temperature dependent acid site measured from Py-FT-IR of $Ni_{0.9}V_{0.1}WO_4$, ABS-contaminated $Ni_{0.9}V_{0.1}WO_4$ (e) FT-IR results of ABS-contaminated (solid line) and pristine (dotted line) $Ni_{1-x}V_xWO_4$. (f) and (g) AC conductivity of pristine $Ni_{0.95}V_{0.05}WO_4$, $Ni_{0.9}V_{0.1}WO_4$, and ABS-contaminated samples at different temperatures. (h-j) Chemisorption results of the ABS-contaminated $Ni_{1-x}V_xWO_4$ samples (colored area) compared with pristine samples (dotted line). (h) H_2-TPR, (i) NH_3-TPD, and (j) O_2-TPO results. The ABS-contaminated V_2O_5-WO_3 chemisorption results are in Fig. S 10.

200 °C in $Ni_{0.9}V_{0.1}WO_4$. However, the O_2-TPO results in Fig. 4c only show a linear background signal without O_2 desorption peaks in $Ni_{1-x}V_xWO_4$, indicating a one-way catalytic cycle. In contrast, strong peaks around 610 °C are observed for V_2O_5-WO_3 compounds, as previously reported [39]. FT-IR peaks (near 3400 and 1500 cm^{-1}) for hydroxyl (-OH) group were observed both in $Ni_{0.95}V_{0.05}WO_4$ and $Ni_{0.9}V_{0.1}WO_4$ (Fig. 4d), and the fraction of oxygen vacancy, quantified by XPS (Fig. S6), was almost same in these two samples. Hence, the presence of a substitutional V dopant activates the chemical reaction on the $NiWO_4$ SCES matrix, manifesting in multiple reduction steps. However, the absence of an oxidized step after synthesizing $Ni_{1-x}V_xWO_4$ under an air environment indicates that the cation valence state does not exceed + 2.α for Ni and V, underscoring the preservation of electron correlation between magnetic cations, as measured by the XPS results (Fig. S6).

To unravel the underlying reason for the boosted deNOx reaction, even on a catalyst surface obstructed by ABS (Fig. 1a), we performed additional XPS, FT-IR, and chemisorption tests using artificially made ABS-contaminated $Ni_{1-x}V_xWO_4$. The XPS results of the poisoned $Ni_{1-x}V_xWO_4$ (displayed in Fig. 5a-c) exhibit similar characteristics to the clean surface samples, indicating the preservation of the valence states of Ni, V, and W in $Ni_{1-x}V_xWO_4$.

The Pyrodine-FT-IR (Py-FT-IR) results for $Ni_{0.95}V_{0.05}WO_4$ and $Ni_{0.9}V_{0.1}WO_4$ at room temperature (shown in Fig. S9) reveal that pristine $Ni_{1-x}V_xWO_4$ exclusively exhibits Lewis acid sites. Whereas, ABS-contaminated $Ni_{1-x}V_xWO_4$ includes Brønsted acid sites, originating from the sulfuric acid of ABS on the $Ni_{1-x}V_xWO_4$ surface. We measured also the temperature dependence PY-FT-IR of $Ni_{0.9}V_{0.1}WO_4$ as shown in Fig. 5d. The pristine sample predominantly exhibits Lewis sites, while the ABS-contaminated sample shows mixed Lewis and Brønsted acid sites. On the other hand, the Brønsted site is weakly activated with increasing temperature in the pristine $Ni_{0.9}V_{0.1}WO_4$, whereas the Brønsted site is deactivated with increasing temperature in the ABS-contaminated sample. Therefore, the dominant Lewis acid in $Ni_{1-x}V_xWO_4$ indicates the NH_3 adsorption on V rather than NH_4^+ adsorption on O, suggesting dominant NH_3 adsorption mechanism via electron transfer between NH_3 and V in NWO_4 SCES matrix for deNOx measured temperature range. In the FT-IR spectra (Fig. 5e), peak broadening was observed both in $Ni_{0.95}V_{0.05}WO_4$ and $Ni_{0.9}V_{0.1}WO_4$ after ABS contamination. This suggests the change in dipole interaction due to the generation of bonding between ABS and $Ni_{1-x}V_xWO_4$. However, the broader peak shape is due to the contamination on the catalyst surface and suggests the relatively weaker electron correlation by lower dipole-dipole interaction between cations. In the 1000 – 4000 cm^{-1} region (Fig. 5f), not only are the -NH_3 and -SO_4 groups presented, but also a noticeable reduction in the -OH group due to the adsorption -NH_3 group instead of -OH as referred to by Brønsted acid site via Py-FT-IR. The weaker electron correlation between Ni and V in SCES $Ni_{1-x}V_xWO_4$ is demonstrated by enhanced electron transfer measured, as measured by AC conductivity. The higher AC conductivity observed in ABS-contaminated $Ni_{1-x}V_xWO_4$ compared to pristine $Ni_{1-x}V_xWO_4$ (Fig. 5g and h) indicates improved electron transfer due to the asymmetric electron/hole pair of cations in the more acidified environment.

The higher acidified cations in ABS-contaminated samples exhibit different reduction and oxidation points than pristine samples, as shown in Fig. 5h-j (H_2-TPR, NH_3-TPD, and O_2-TPO results). In H_2-TPR (Fig. 5h), a strong single peak around 600 °C is composed of overlapped reduction steps on ABS-contaminated $Ni_{1-x}V_xWO_4$. The NH_3-TPD (Fig. 5i) shows a distinct trend of NH_3 desorption between the ABS-contaminated sample (solid area) and the pristine sample (dotted line). The higher NH_3 desorption point around 100 °C in the pristine sample becomes weaker, but a larger NH_3 desorption peak of around 250 °C is measured in the ABS-contaminated samples. The large peak of around 250 °C for all samples is related to a combination of the ABS decomposition temperature (~300 °C) and enhanced NH_3 desorption at 200 – 300 °C. Nevertheless, the higher intensity of NH_3 desorption in the overall range of $Ni_{1-x}V_xWO_4$ demonstrates the boosted catalytic reaction of $Ni_{1-x}V_xWO_4$ compared to the deteriorated NO_x conversion of V_2O_5-WO_3 compound under the same SO_x environment (Fig. 3a and Fig. S2). Thus, the reduced -OH group as shown in FT-IR results in Fig. 5e, and increasing NH_3 desorption in medium and strong acid sites suggest that the ABS-contaminated $Ni_{1-x}V_xWO_4$ mainly follows the Lewis acid model, which involves a reduction reaction primarily using electron transfer. The O_2-TPO results (Fig. 5j) imply the mechanism behind the boosted deNO_x performance. The relatively lower O_2-TPO signal of V_2O_5-WO_3 in Fig. S10 is related to the weaker reduction/oxidation cycle that leads to deteriorated deNO_x performance (in Fig. S11). However, the emergence of the small peaks on the ABS-contaminated $Ni_{1-x}V_xWO_4$ suggests the opening the reduction/oxidation cycle due to higher carrier transfer between the weaker correlation between $Ni^{+2.\alpha-\gamma}$ and acidified $V^{+2.\alpha+\delta}$ as asymmetric electron/hole pair than strong electron correlation between $Ni^{+2.\alpha}$ and $V^{+2.\alpha}$ in pristine $Ni_{1-x}V_xWO_4$ as described in Fig. 1c.

4. Conclusion

In this study, we introduce a novel V-containing $NiWO_4$ matrix which exhibits the capability to counteract the degraded denitration performance in commercial V_2O_5-based catalysts under the influence of SO_x. This discovery is realized through the strategic control of the V valence state within a strongly correlated electron system. Our design entails substitutional V in $NiWO_4$, resulting in a persistent valence state of V as + 2 – + 3, even in the presence of SO_x. This leads to a boosted catalytic reaction with high N_2 selectivity, benefitting from the increased accessibility of catalytic sites due to lower electron correlation, stemming from the higher valence state of acidified V on the ABS-contaminated surface. Our findings reveal that $Ni_{1-x}V_xWO_4$, when contaminated with ABS salt, demonstrates a stable reduction/oxidation cycle and exhibits superior NH_3 absorption, resulting in improved catalytic reactions. Considering the fine-tuning the catalytic particle size to a few nanometers using impregnation and optimizing the appropriate support drive the higher NO_x conversion performance, the $Ni_{1-x}V_xWO_4$ exhibit the potential after optimization to approach toward practical efficiency in relatively high SO_x concentrated environments, such as the oil refining industry. By employing intrinsic cation charge control within a strongly correlated electron system, we not only provide inspiration for the development of selective catalytic reduction materials beyond conventional MOs but also pave the way for a deeper exploration into the underlying mechanisms governing catalytic reactions in strongly correlated electron systems.

CRediT authorship contribution statement

Bang Joonho: Formal analysis, Investigation. **Lee Seung Yong:** Conceptualization, Data curation, Formal analysis, Investigation, Project administration, Supervision, Writing – original draft, Writing – review & editing. **Suh June Won:** Formal analysis, Investigation, Writing – original draft. **Jeong Bo Ra:** Formal analysis, Investigation. **Kim Hong-Dae:** Formal analysis, Investigation. **Lee Jung-Woo:** Formal analysis, Investigation. **Lee Kimoon:** Conceptualization, Data curation, Formal analysis, Writing – original draft, Writing – review & editing. **Choi Myung Sik:** Formal analysis, Investigation. **Jin Changhyun:** Formal analysis, Investigation. **Jeong Si Hoon:** Formal analysis, Investigation. **Park Gi Hyun:** Formal analysis, Investigation. **Sun-Dong Kim:** Formal analysis, Investigation. **Lee Kyu Hyoung:** Conceptualization, Data curation, Formal analysis, Investigation, Project administration, Supervision, Writing – original draft, Writing – review & editing. **Park Jihye:** Investigation, Methodology. **Kim Sung Eun:** Formal analysis, Investigation. **Kim Hak Joo:** Formal analysis, Investigation. **Lee Hyesung:** Formal analysis, Investigation. **Ji Yunseong:** Formal analysis, Investigation.

Declaration of Competing Interest

The authors declare that they have no known competing financial interests or personal relationships that could have appeared to influence the work reported in this paper.

Data availability

Data will be made available on request.

Acknowledgments

This research was supported by Samsung Research Funding & Incubation Center of Samsung Electronics under Project Number SRFC-MA1902-03. This work was also supported by the National Research Foundation of Korea (NRF) grant funded by the Korea government (MSIT) 2022R1A2C2005210. Seung Yong Lee was supported by the Korea Initiative for fostering University of Research and Innovation (KIURI) Program of the National Research Foundation (NRF) funded by the Korean government (MSIT) 2020M3H1A1077207 and 2022R1I1A1A0107118312.

Appendix A. Supporting information

Supplementary data associated with this article can be found in the online version at doi:10.1016/j.apcatb.2023.123540.

References

[1] L. Han, S. Cai, M. Gao, J.-Y. Hasegawa, P. Wang, J. Zhang, L. Shi, D. Zhang, Selective catalytic reduction of NO_x with NH_3 by using novel catalysts: state of the art and future prospects, Chem. Rev. 119 (2019) 10916–10976.
[2] C.K. Lambert, Current state of the art and future needs for automotive exhaust catalysis, Nat. Catal. 2 (2019) 554–557.
[3] G. He, Z. Lian, Y. Yu, Y. Yang, K. Liu, X. Shi, Z. Yan, W. Shan, H. He, Polymeric vanadyl species determine the low-temperature activity of V-based catalysts for the SCR of NO_x with NH_3, Sci. Adv. 4 (2018), eaau4637.
[4] S.G. Lee, H.J. Lee, I. Song, S. Youn, D.H. Kim, S.J. Cho, Suppressed N_2O formation during NH_3 selective catalytic reduction using vanadium on zeolitic microporous TiO_2, Sci. Rep. 5 (2015) 12702.
[5] W. Qu, X. Liu, J. Chen, Y. Dong, X. Tang, Y. Chen, Single-atom catalysts reveal the dinuclear characteristic of active sites in NO selective reduction with NH_3, Nat. Commun. 11 (2020) 1532.
[6] D.W. Kwon, J. Choi, K.B. Nam, H.P. Ha, New insight into the role of Mo–Sb addition towards VMoSbTi catalysts with enhanced activity for selective catalytic reduction with NH_3, Chem. Eng. J. 428 (2022), 132078.
[7] J. Kim, D. Kim, H.P. Ha, Investigating multi-functional traits of metal-substituted vanadate catalysts in expediting NO_x reduction and poison degradation at low temperature, J. Hazard. Mater. 397 (2020), 122671.
[8] Y. Inomata, H. Kubota, S. Hata, E. Kiyonaga, K. Morita, K. Yoshida, N. Sakaguchi, T. Toyao, K.-I. Shimizu, S. Ishikawa, W. Ueda, M. Haruta, T. Murayama, Bulk tungsten-substituted vanadium oxide for low temperature NO_x removal in the presence of water, Nat. Commun. 12 (2021) 557.
[9] J. Liu, R.-Y. Guo, M.-Y. Li, P. Sun, S.-M. Liu, W.-G. Pan, S.-W. Liu, X. Sun, Enhancement of the SO_2 resistance of Mn/TiO_2 SCR catalyst by Eu modification: a mechanism study, Fuel 223 (2018) 385–393.
[10] D.W. Kwon, K.H. Park, H.P. Ha, S.C. Hong, The role of molybdenum on the enhanced performance and SO_2 resistance of V/Mo-Ti catalysts for NH_3-SCR, Appl. Surf. Sci. 481 (2019) 1167–1177.
[11] Q. Yan, S. Chen, C. Zhang, Q. Wang, B. Louis, Synthesis and catalytic performance of $Cu_1Mn_{0.5}Ti_{0.5}O_x$ mixed oxide as low temperature NH_3 -SCR catalyst with enhanced SO_2 resistance, Appl. Catal. B 238 (2018) 236–247.
[12] D.W. Kwon, D.H. Kim, S. Lee, J. Kim, H.P. Ha, A dual catalytic strategy by the nature of the functionalization effect as well as active species on vanadium-based catalyst for enhanced low temperature SCR, Appl. Catal. B 289 (2021), 120032.
[13] X. Wang, X. Du, S. Liu, G. Yang, Y. Chen, L. Zhang, X. Tu, Understanding the deposition and reaction mechanism of ammonium bisulfate on a vanadia SCR catalyst: a combined DFT and experimental study, Appl. Catal. B 260 (2020), 118168.
[14] K. Guo, J. Ji, W. Song, J. Sun, C. Tang, L. Dong, Conquering ammonium bisulfate poison over low-temperature NH_3-SCR catalysts: a critical review, Appl. Catal. B 297 (2021), 120388.
[15] Y. Shu, T. Aikebaier, X. Quan, S. Chen, H. Yu, Selective catalytic reaction of NO_x with NH_3 over Ce–Fe/TiO_2 -loaded wire-mesh honeycomb: resistance to SO_2 poisoning, Appl. Catal. B 150–151 (2021) 630–635.
[16] I. Song, H. Lee, S.W. Jeon, I.A.M. Ibrahim, J. Kim, Y. Byun, D.J. Koh, J.W. Han, D. H. Kim, Simple physical mixing of zeolite prevents sulfur deactivation of vanadia catalysts for NO_x removal, Nat. Commun. 12 (2021) 901.
[17] Q. Wu, X. Chen, J. Mi, S. Cai, L. Ma, W. Zhao, J. Chen, J. Li, The absence of oxygen in sulfation promotes the performance of the sulfated CeO_2 catalyst for low-temperature selective catalytic reduction of NO_x by NH_3: redox property versus acidity, ACS Sustain. Chem. Eng. 9 (2021) 967–979.
[18] Z. Huang, Z. Zhu, Z. Liu, Combined effect of H_2O and SO_2 on V_2O_5/AC catalysts for NO reduction with ammonia at lower temperatures, Appl. Catal. B 39 (2002) 361–368.
[19] E. Morosan, D. Natelson, A.H. Nevidomskyy, Q. Si, Strongly correlated materials, Adv. Mater. 24 (2012) 4896–4923.
[20] R.S. Kate, S.A. Khalate, R.J. Deokate, Overview of nanostructured metal oxides and pure nickel oxide (NiO) electrodes for supercapacitors: a review, J. Alloy. Compd. 734 (2018) 89–111.
[21] F. Cesare, R. Michele, M. Setvin, U. Diebold, Polarons in materials, Nat. Rev. Mater. 6 (2021) 560–586.
[22] A.S. Alexandrov. Polarons in Advanced Materials, Springer, 2007.
[23] A. Bhargava, R. Eppstein, J. Sun, M.A. Smeaton, H. Paik, L.F. Kourkoutis, D. G. Schlom, M.C. Toroker, R.D. Robinson, Breakdown of the small-polaron hopping model in higher-order spinels, Adv. Mater. 32 (2020) 2004490.
[24] P. Watthaisong, S. Jungthawan, P. Hirunsit, S. Suthirakun, Transport properties of electron small polarons in a V_2O_5 cathode of Li-ion batteries: a computational study, RSC Adv. 9 (2019) 19483.
[25] B. Jacqueline, C. Andrea, G. Victor, H. Mohammad, R. Angel, Strongly correlated electron–photon systems, Nature 606 (2022) 41–48.
[26] S.G. Park, K.H. Lee, J.-H. Lee, G. Bang, J. Kim, H.J. Park, M.S. Oh, S. Lee, Y.-H. Kim, Y.-M. Kim, H. Hosono, J. Bang, K. Lee, Improved polaronic transport under a strong Mott–Hubbard interaction in Cu-substituted NiO, Inorg. Chem. Front. 7 (2020) 853–858.
[27] N. Morlanés, S. Sayas, G. Shterk, S.P. Katikaneni, A. Harale, B. Solami, J. Gascon, Development of a Ba–CoCe catalyst for the efficient and stable decomposition of ammonia, Catal. Sci. Technol. 11 (2021) 3014.
[28] P. Xinyan, H. Chao, D. Jun, Y. Liu, Uniform cobalt grafted on vanadium nitride as a high efficient oxygen evolution reaction catalyst, Int. J. Hydrog. Energy 47 (2022) 4386–4393.
[29] B.H. Toby, R.B. Von Dreele, GSAS-II: the genesis of a modern open-source all purpose crystallography software package, J. Appl. Crystallogr. 46 (2013) 544–549.
[30] K. Momma, F. Izumi, VESTA 3 for three-dimensional visualization of crystal, volumetric and morphology data, J. Appl. Crystallogr. 44 (2011) 1272–1276.
[31] P.E. Blöchl, Projector augmented-wave method, Phys. Rev. B Condens. Matter 50 (1994) 17953–17979.
[32] J.P. Perdew, K. Burke, M. Ernzerhof, Generalized gradient approximation made simple, Phys. Rev. Lett. 77 (1996) 3865–3868.
[33] G. Kresse, J. Furthmüller, Efficient iterative schemes for ab initio total-energy calculations using a plane-wave basis set, Phys. Rev. B Condens. Matter 54 (1996) 11169–11186.
[34] S.L. Dudarev, G.A. Botton, S.Y. Savrasov, C.J. Humphreys, A.P. Sutton, Electron-energy-loss spectra and the structural stability of nickel oxide: an LSDA+U study, Phys. Rev. B Condens. Matter 57 (1998) 1505–1509.
[35] H. Chen, J.H. Harding, Nature of the hole states in Li-doped NiO, Phys. Rev. B Condens. Matter 85 (2012), 115127.
[36] Y.L. Oliveira, M.J.S. Costa, A.C.S. Jucá, L.K.R. Silva, L.S. Cavalcante, Structural characterization, morphology, optical and colorimetric properties of $NiWO_4$ crystals synthesized by the co-precipitation and polymeric precursor methods, J. Mol. Struct. 1221 (2020), 128774.
[37] S.D. Ramarao, V.R.K. Murthy, Structural, Raman spectroscopic and microwave dielectric studies on $Ni_{1-x}(Zn_{1/2}Zr_{1/2})_xW_{1-x}Nb_xO_4$ ceramic compounds with wolframite structure, Dalton Trans. 44 (2015) 2311–2324.
[38] H. Harshan, K.P. Priyanka, A. Sreedevi, A. Jose, T. Varghese, Structural, optical and magnetic properties of nanophase $NiWO_4$ for potential applications, Eur. Phys. J. B 91 (2018) 287.
[39] S. Besselmann, C. Freitag, O. Hinrichsen, M. Muhler, Temperature-programmed reduction and oxidation experiments with V_2O_5/TiO_2 catalysts, Phys. Chem. Chem. Phys. 3 (2001) 4633–4638.